AIAA 2003-1102
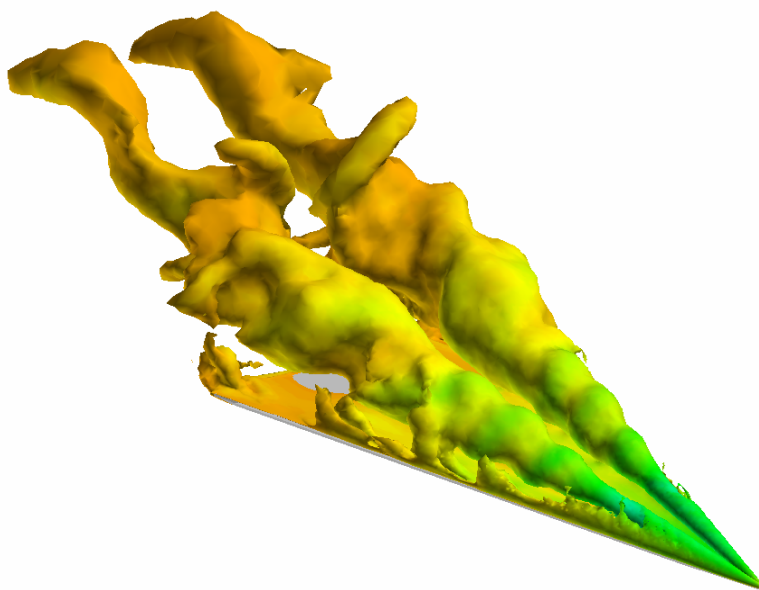
Computational Simulation and PIV Measurements of the Laminar Vortical Flowfield for a Delta Wing at High Angle of Attack

Russell M. Cummings, Scott A. Morton, Stefan G. Siegel
Department of Aeronautics
United States Air Force Academy
USAF Academy, CO 80840

41st Aerospace Sciences Meeting & Exhibit
6-9 January, 2003
Reno, Nevada

Computational Simulation and PIV Measurements
of the Laminar Vortical Flowfield for a Delta Wing at High Angle of Attack

Russell M. Cummings,* Scott A. Morton,[†] and Stefan G. Siegel[‡]

Department of Aeronautics
United States Air Force Academy
USAF Academy, CO 80840

Abstract

The low-speed, laminar flowfield for a 70°-sweep delta wing is investigated. Solutions to the unsteady, three-dimensional, compressible Navier-Stokes equations were obtained on an unstructured grid to match results from an experiment performed in a water tunnel. The experiment was conducted with the delta wing at an angle of attack of 35° and the freestream flow at a root-chord Reynolds number of 40,700. The computational results are analyzed and compared with the experimental results in order to show how computations and experiments can be conducted in a synergistic fashion. Details about the primary vortex location, vortex burst, secondary vortex, and shear layer interaction are shown and discussed.

Nomenclature

b	Local wing span
c	Wing root chord, 298 mm
C_μ	Oscillatory momentum coefficient, $2(H/c)(\langle v'\rangle/U_\infty)^2$
f	Frequency
F^+	Nondimensional frequency, fc/U_∞
H	Forcing slot height, 1.5 mm
M	Mach number
Re	Reynolds number, $U_\infty c/v_\infty$
St	Strouhal number, fc/U_∞
t	Time
T	Period of blowing and suction cycle, 1.352 s
u, v, w	Velocity components along x, y, z axes
$\langle v'\rangle$	R.M.S. amplitude of blowing velocity
U_∞	Freestream velocity, 0.126 m/s
x, y, z	Cartesian coordinates fixed to the wing
α	Wing angle of attack, 35°
υ	Kinematic viscosity
∞	Freestream conditions

* Distinguished Visiting Professor, on sabbatical leave from the Aerospace Engineering Department, California Polytechnic State University, Associate Fellow AIAA.
[†] Associate Professor, Associate Fellow AIAA.
[‡] Postdoctoral Researcher, Member AIAA.

Introduction

The need to improve fighter aircraft and missile maneuverability has inspired extensive study of the flow past a variety of geometries, including delta wings and fuselage forebodies (see Refs. 1 and 2 for example). In addition, numerous studies have centered on methods to delay or control vortex breakdown, which include a variety of blowing, suction, and various combinations of other pneumatic flow control concepts.[3-8] In recent years, the efficacy of oscillatory flow excitation with zero net mass flux and non-zero momentum flux has been shown. Oscillatory flow oscillation is more effective for delaying separation from a lifting surface or promoting reattachment of initially separated flow, relative to steady blowing methods traditionally used for this purpose.

Guy, et al.,[9-13] have recently experimented with oscillatory flow excitation at the leading edge of a delta wing. They have investigated the spatial effects of periodic suction and blowing (PSB) on delta wing vortex breakdown by wind tunnel and water tunnel experimentation. The investigation focused on extending the aerodynamic envelope of a 70°-sweep delta wing by active control of the vortical flow over the wing. It was shown that periodic suction and blowing delays vortex breakdown and wing stall, and increases lift at high angles of attack. Key control parameters were defined and optimum values of these parameters were established. The experimental investigation indicates that periodic suction and blowing delays vortex breakdown by approximately 0.2 chord lengths, delays stall by approximately 10°, and increases lift by 40% at an angle of attack of 40°.

Following these encouraging results, a continuation of the research was undertaken at the USAF Academy. It was aimed at giving an in-depth understanding of the mechanism through which periodic suction and blowing affects the structure and behavior of the leading edge vortex. A first step in this direction was taken by Morton, et al.,[13] who numerically simulated the flow about a delta wing with and without periodic suction and blowing. More recent studies have also been conducted in a water tunnel at the USAF Academy, which form the basis for this article.[14] The purpose of this investigation is to determine how well numerical simulations of the delta wing flowfield with and without leading-edge blowing and suction can match experimental measurements. Specifically, the eventual goal is to show how computations can aid in improving the experimental method by giving insight into details about the flowfield that can aid experimentalists in designing their measurements to best take advantage of limited apparatus and time.

Computational Method

The unstructured flow solver Cobalt was chosen because of its speed and accuracy; Cobalt is a commercial version of $Cobalt_{60}$. Cobalt solves the Navier-Stokes equations, including an improved spatial operator and improved temporal integration. The code has been validated on a number of problems, including the Spalart-Allmaras model (which forms the core of the DES model).[15] Tomaro, et al., converted $Cobalt_{60}$ from explicit to implicit, enabling CFL numbers as high as one million.[16] Grismer, et al., then parallelized the code, yielding a linear speedup on as many as 1024 processors.[17] Forsythe, et al., provided a comprehensive testing and validation of the RANS models, including the Spalart-Allmaras, Wilcox k-ω, and Menter's turbulence models.[18]

A previous numerical study computed the flow over a flat-plate, semi-span delta wing with a leading-edge sweep of 70° and a 25° bevel on the lower surface in a wind tunnel.[19-20] The wing had a root chord of 0.74 m with a 3 mm slot extending the entire length of the leading edge. The results of the wind tunnel experiment showed a significant impact of periodic blowing and suction, which led to additional experiments in a water tunnel, and eventually to a desire to numerically model the water tunnel experimental results.

Solutions to the unsteady, three-dimensional, compressible Navier-Stokes equations with a laminar-flow assumption were obtained on two unstructured grids—details for the study may be found in Ref. 21. Grids from the wind tunnel computations were first modified to match the water tunnel model root chord of 0.298 m. A semi-span coarse grid was used that contained 133,000 points and 591,000 cells, and the fine grid contained 252,000 points and 1.24 million cells. Approximately 10% of each grid was made up of prisms near the surface, while the remaining cells were tetrahedra. Results from both grids will be shown and discussed. Solutions were obtained at an angle of attack $\alpha = 35^o$, with and without periodic suction and blowing through the leading-edge slot. Blowing and suction was applied normal to the leading edge and parallel to the upper surface of the wing from a slot of height, $H = 1.5$ mm. The experimental free stream velocity was 0.126 m/s and the corresponding root-chord Reynolds number was 40,700. The freestream Mach number for the computations was set to $M_\infty = 0.1$, with the freestream pressure and temperature chosen to match the Reynolds number of the experiment. Periodic blowing and suction was applied at a non-dimensional frequency of $F^+ = 1.75$ and the momentum coefficient was $C_\mu = 0.004$—these values matched those used in the water tunnel experiment. The grids were used to obtain solutions for the case without blowing after running the solution for 4000 to 5000 iterations to insure that all start-up instabilities were damped out. The periodic blowing and suction solutions were started from the well established non-blowing solutions.

Experimental Setup

A flat-plate delta wing with a leading-edge sweep of 70° and a 25° bevel on the lower surface, was investigated in the USAF Academy 38 cm × 110 cm free-surface water tunnel. The wing has a chord length of 298 mm, is hollow and has a 1.5 mm slot along its leading edge. The wing was sting-mounted and placed inverted at an angle of attack of 35° in the water tunnel.

To perturb the shear layer originating at the leading edge of the delta wing, a semi-spherical rubber cap was used as an oscillatory blowing and suction flow actuator. It was moved back and forth by a connecting rod, eccentrically mounted on a disk that was driven by a 560 W DC motor. The water displacement produced by the moving cap was channeled through a tube 2 cm in diameter to the hollow wing and to the length of the slot in its leading edge. With this setup, as with any oscillatory flow control method, fluid is drawn into the actuator over half of the sinusoidal cycle, and ejected over the

other half ($V = V_o \sin \omega t$). The phase during the forcing cycle is determined by the position of the rotating disk flywheel, which features an adjustable optical pickup to synchronize the data acquisition with a particular phase of the forcing cycle. A forcing cycle starts at 0° with the blowing phase which extends to 180°. The suction portion between 180° and 360° completes the cycle.

To sample the flow, a Dantec *Flowmap* two-component PIV system with a New Wave *Gemini* 125 mJ Nd:Yag laser operating at 532 *nm* was used. A Kodak *Megaplus* ES 1.0 CCD camera (1000 × 1000 pixel resolution) was mounted downstream of the delta wing, to visualize the flow in a plane perpendicular to the model suction surface. A special plexiglass viewing box was used to facilitate viewing of planes perpendicular to the wing, avoiding the inherent refraction from the water surface. For measurements in a plane at a constant spanwise location, the laser was set up below the test section illuminating the flow from below, while the camera imaged the flow through the side window.

The operating parameters for the PIV system were kept constant throughout the study. Seeding was provided using 20 μm Polyethylene particles. The system operated in cross correlation mode using two images, which were correlated in the frequency domain. Before correlation, a 3 × 3 Low pass filter was used to widen the particle images. A 32 × 32 pixel interrogation area was used, and the images were processed with 75% overlap yielding a raw vector field of 123 × 123 vectors. The vector acceptance criteria were a peak ratio of at least 1.2, and 25% maximum velocity variation from neighboring vectors.

PIV images were phase-referenced to the forcing mechanism, to allow phase averaging of ten images, thus increasing signal-to-noise ratio of the data. Data sets were obtained every ten degrees through the 360° forcing cycle. Basic data reduction was done using the *Flowmap* PIV software for vector validation, spatial moving average smoothing in a 3 × 3 vector area and averaging of the ten data sets. The data was then imported into LabVIEW-based post processing software for further data reduction and analysis. Details of the results of this study can be found in Ref. 14.

Results and Discussion

Spatial and Temporal Convergence Study

In order to determine the appropriate grid density and time step for the numerical simulations, a study was carried out for the highly unsteady flowfield caused by the burst vortices above the delta wing at $\alpha = 35^o$. Details about the convergence study may be found in Ref. 21. Solutions for the delta wing using the coarse grid were obtained at various time steps, including $\Delta t = 0.020$, 0.010, 0.005, and 0.0025. The power spectrum density of the normal force from the coarse grid solutions were obtained using MATLAB and plotted in Fig. 1. The four time steps shown each produce a different primary frequency (shown as the wave number, which is the inverse of the Strouhal number). Clearly, the dominant unsteady features of the flow are not properly resolved if each time step yields a different vortex frequency. In order to determine whether or not a converged time step is being approached, the log of the wave number for each time step is plotted against the log of the time step in Fig. 2. Notice that a secondary frequency becomes apparent as the time step is decreased; the cause of the secondary frequency will be discussed later. While the smallest time steps show convergence, the coarseness of the grid probably will not allow for all flow features to be captured.
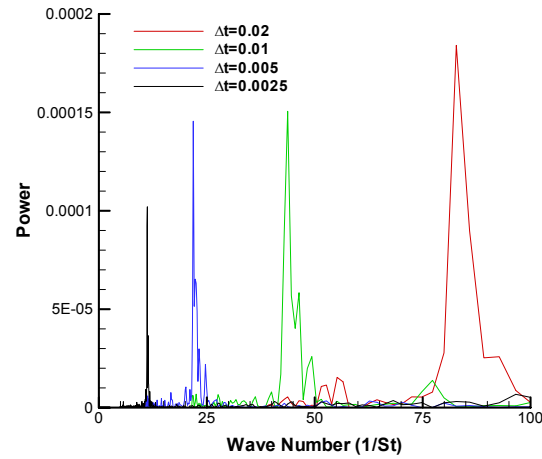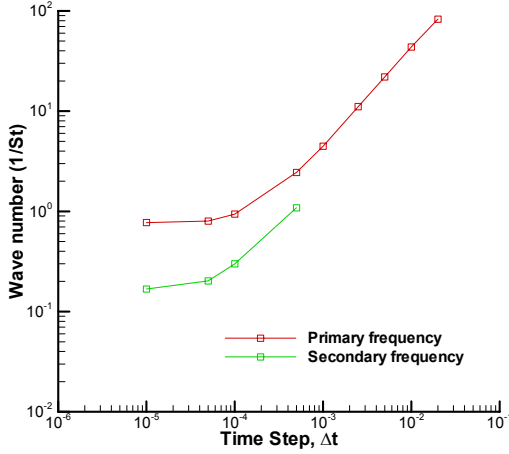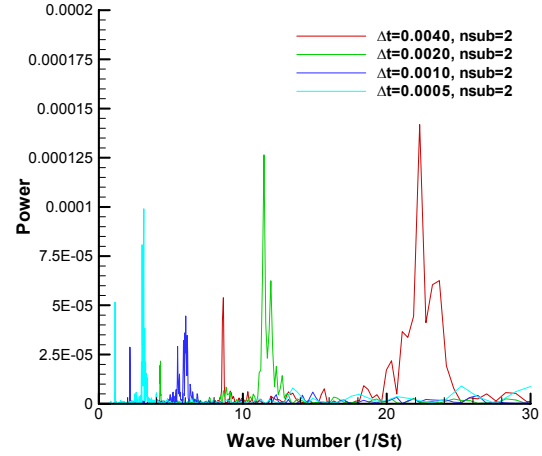

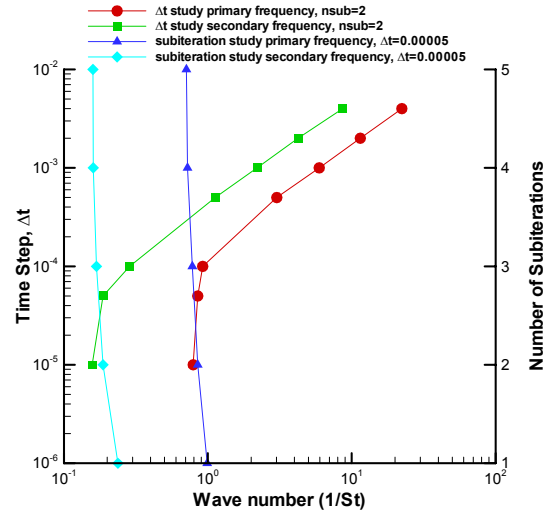**Figure 1. Power spectrum density for coarse grid at various time steps.**

Figure 2. Wave number variation with time step for the coarse grid.

Figure 3. Power spectrum density for fine grid at various time steps and two Newton subiterations.

A similar study was then conducted using the fine grid. Power spectrum densities for four of the time steps (starting with values comparable to those used for the coarse grid) are shown in Fig. 3. The computations were all performed for the same physical time (10 seconds) by varying the number of iterations for each time step (2500 iterations for $\Delta t =$ 0.004, 5000 iterations for $\Delta t = 0.002$, etc.), and each computation was completed with two Newton sub-iterations. The detail of the frequency spectrum is more complex for the fine grid when compared with the coarse grid, as evidenced by the multiple power spikes in the vicinity of the primary frequency (compare Fig. 3 with Fig. 1).

These results are consolidated and shown as a function of time step and number of subiterations in Fig. 4. As can be clearly seen, both the primary and secondary frequencies converge to a constant value as the time step decreases. In addition, the converged frequencies are the same as those achieved with the coarse grid (see Fig. 2), which means that the fine grid resolution is more than adequate for resolving the essential features of the flowfield. A notable feature is that the non-dimensional frequency of the blowing and suction is 1.75 (which corresponds to a wave number of 0.571), which lies between the primary and secondary frequencies for the non-blowing flowfield; the flow features associated with the blowing should therefore be well modeled with this grid and time step.


Figure 4. Wave number variation with time step and number of subiterations for the fine grid.

An additional time convergence study was then performed to determine the effect of the number of Newton subiterations on the solution. Figure 4 also shows the wave number for five Newton subiteration levels (nsub = 1, 2, 3, 4, and 5), all at a time step of $\Delta t = 0.00005$. Once again, two dominant frequencies can be seen, with the wave number for both the primary and secondary frequencies decreasing with increasing number of Newton subiterations. In fact, the secondary frequency seems to have nearly converged, while the primary frequency is very nearly converged at nsub = 4. These studies (time step and Newton subiteration) have shown that the essential features of the flowfield are appropriately modeled with a time step of $\Delta t = 0.00005$ and a Newton subiteration level of nsub = 3. All remaining comparisons for non-blowing cases will be made for

computations made at these conditions. Certainly, slightly improved solutions would be obtained by using $\Delta t = 0.00001$ and nsub = 3; these conditions are used for the following periodic suction and blowing cases. Using these values the flow exhibits a primary frequency of approximately 1.3 and a secondary frequency of approximately 6.0. The following discussions will attempt to determine the causes of these frequencies.

Primary and Secondary Vortex Frequencies

In order to determine the cause of the frequencies seen in Fig. 3, "pressure taps" were placed in the computational flowfield along the cores of the primary and secondary vortices. In both cases, the taps were located both before and after observed breakdown locations. Figure 5 shows the frequency history for six pressure taps along the core of the primary vortex, and Fig. 6 shows the frequency history for six pressure taps along the secondary vortex. Tap #1 is located nearest to the vertex of the delta wing, and Tap #6 is beyond the vortex breakdown location (see Table 1 for the longitudinal locations of the pressure taps).
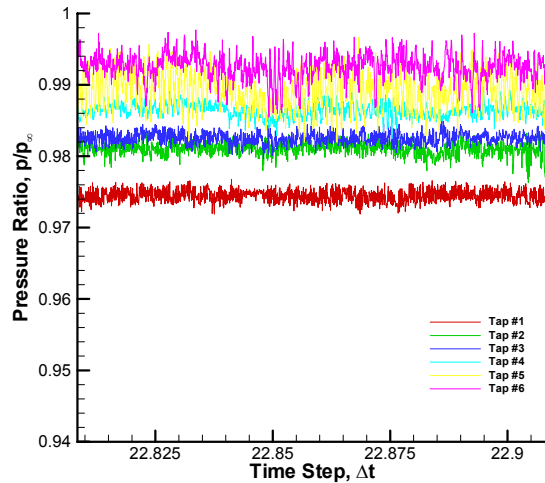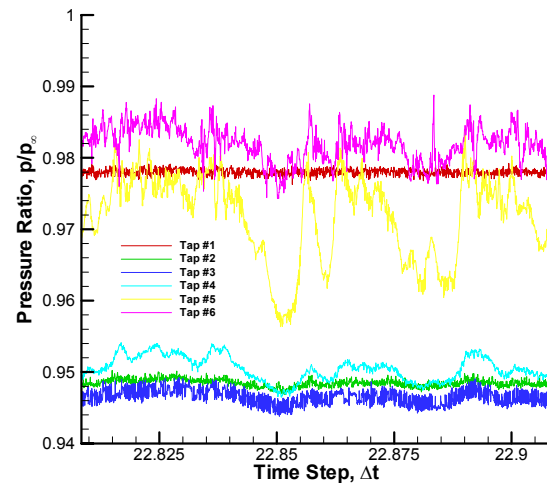

Figure 5. Numerical prediction pressure histories along the core of the primary vortex (Tap #1 is closest to the delta wing vertex).

As can be seen in Fig. 5, the pressure frequencies increase in average values as the tap locations move further aft, showing the adverse pressure gradient normally seen on the upper surface of a wing. The frequency content at each tap location also changes with tap position as well. There is no dominant frequency for the first three pressure tap locations on the primary vortex (Taps #1 through #3). However, a PSD analysis of the pressure variations for Taps #4 through #6 showed that the primary non-dimensional

frequency is approximately 8.5. After breakdown a different pressure history is seen, with the primary non-dimensional frequency decreasing to approximately 1.35. These frequencies were confirmed with animations of the flowfield, and match the shedding evident from the leading edge and the winding of the vortex after breakdown (F^+ = 1.35).

Figure 6 shops the pressure histories along the secondary vortex. The most forward tap (Tap #1) along the secondary vortex shows pressures that are comparable to those seen in the primary vortex (compare Tap #1 in Fig. 6 with Tap #1 in Fig. 5). However, as the secondary vortex passes through Tap #2, #3, and #4, there is a fairly significant drop in pressure. This pressure drop is also accompanied by a noticeable instability in the pressure—the instability becomes more evident as the flow passes from Tap #2 to Tap #4. Finally, a noticeable difference can be seen as the flow reaches Taps #5 and #6. The flow has become more chaotic, with large variations in pressure. PSD analysis shows that Tap #4 has a strong frequency spike at $F+ = 8.5$, which matches well with the frequencies found on the primary vortex. Taps #5 and #6 do not show any single, dominant frequency however. When movies of the flowfield are viewed it becomes apparent that the secondary vortex dissipates quickly and is diffused into the surrounding fluid, which may explain the lack of dominant frequencies at Taps #5 and #6.


Figure 6. Numerical prediction pressure histories along the core of the secondary vortex (Tap #1 is closest to the delta wing vertex).

| Tap #	Primary Vortex Tap x/c	Secondary Vortex Tap x/c
1	.0196	.0192
2	.1655	.1412
3	.1812	.1774
4	.2713	.1812
5	.3350	.3350
6	.3668	.3624

Table 1. Longitudinal location of numerical pressure taps.

When this information is coupled with the flowfield visualization in Fig. 7 the results become more clear. While the primary vortex breaks down and winds at an easily verifiable non-dimensional frequency of F^+ = 1.35, the secondary vortex also breaks down—in fact, the secondary vortex breakdown location is forward of the primary vortex breakdown. This seems to suggest that the secondary vortex breakdown, and whatever may be causing it, is actually causing or affecting the primary vortex breakdown.

Primary vortex breakdown, F+ = 1.35

Secondary vortex breakdown, F+ = 8.5
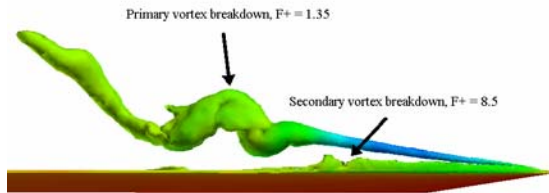
Figure 7. Secondary vortex breakdown and the secondary frequency.

This phenomenon has been previously observed in water tunnel experiments (Ref. 22), Figure 8 shows the results of the water tunnel test on a blade wing at $\alpha = 27^o$, clearly showing the secondary vortex bursting well upstream of the primary vortex.

Secondary vortex burst

Primary vortex burst
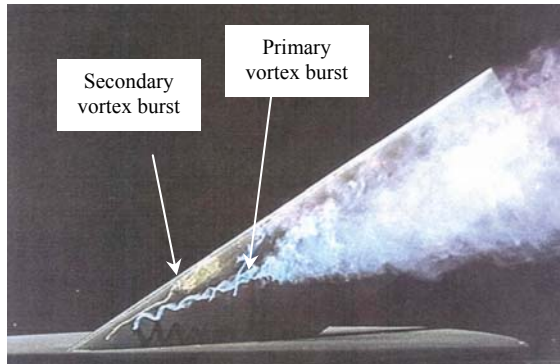
Figure 8. Interaction between secondary vortex and primary vortex (from Ref. 22).
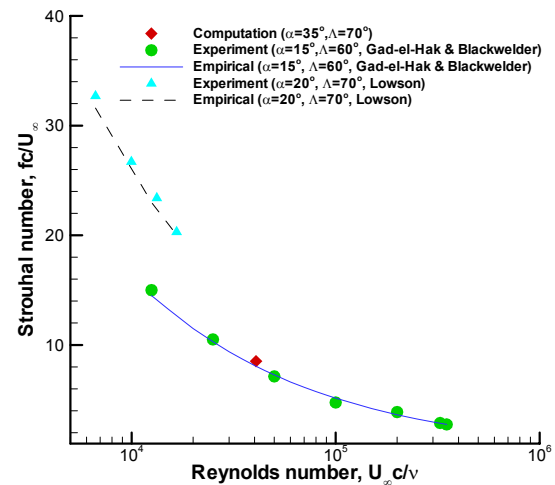
Wing Leading Edge Shedding Frequency

Delta wing leading edge shedding has been studied by, among others, Gad-el-Hak & Blackwelder who used a 60 degree delta wing (Ref. 23) and Lowson who used a 70 degree delta wing (Ref. 24). Both of these studies resulted in collection of shedding frequency data as a function of flow speed, as well as the creation of empirical curve-fits of the Strouhal number for the shedding frequency. Gad-el-Hak & Blackwelder obtained a relation based on data collected between Reynolds numbers between 12,500 and 35,000

$$fc/U_\infty = 1625/\sqrt{Re}$$

and Lowson obtained data for Reynolds numbers between 6,640 and 16,600

$$fc/U_\infty = 2577/\sqrt{Re}$$

The experimental data and empirical curve-fits are shown in Fig. 9. While the present computations are for a delta wing with a 70 degree sweep angle (which matches Lowson's experiment), the angle of attack is higher than either of the experimental results. Gad-el-hak & Blackwelder noted that the shedding frequency was not a function of leading edge sweep angle or leading edge shape, but did find that the frequency was a weak function of angle of attack, with the frequency decreasing with α. The computational leading-edge shedding frequency Strouhal number of approximately 6.0 compares well with the experimental results. This frequency matches the frequency of the secondary vortex breakdown observed previously.


Figure 9. Comparison of numerically predicted leading edge shedding frequency with experimental data and empirical relationships (experimental data from Refs. 23 and 24).

Cause of Secondary Frequency

The secondary frequency predicted with both the coarse and fine grids (Figs. 1 and 3, respectively) was assumed to be caused by the breakdown of the secondary vortex. This breakdown takes place at approximately the same longitudinal location as the primary vortex breakdown (actually slightly ahead, as seen in Fig. 7), but with a frequency approximately five times higher than the frequency caused by the primary vortex windings. It should be noted that the frequency information used in this analysis was taken from the integrated normal force acting on the delta wing, with the primary frequency being caused by the wound vortical structures of the primary vortex as they convect downstream beyond the breakdown location. The pressure taps resulted in a frequency of approximately $F^+ = 8.5$, slightly higher than the value of $F^+ = 6$ found from the integrated normal force predictions.

Further investigation showed that the secondary vortex breakdown is actually directly related to the leading-edge shear layer instability. Figure 10 shows the interaction between the shear layer, the secondary vortex, and the primary vortex, including the primary vortex burst location. The "fingers" of the shear-layer instability directly match the flow structures in the secondary vortex breakdown region as seen in Fig. 7. The visualizations shown here (see Figs. 7, 8, and 10) help to explain the interaction of the various portions of the flowfield—the leading-edge shedding frequency interacts with both the primary and secondary vortex, causing the secondary vortex to breakdown. The instability of both the shear-layer shedding and the secondary vortex breakdown appear to interact with the primary vortex and contribute to the breakdown of that vortex. Certainly, no absolute cause and effect relationships can be deduced by the results shown above, but the evidence seems strong that the three flow structures are inextricably linked.
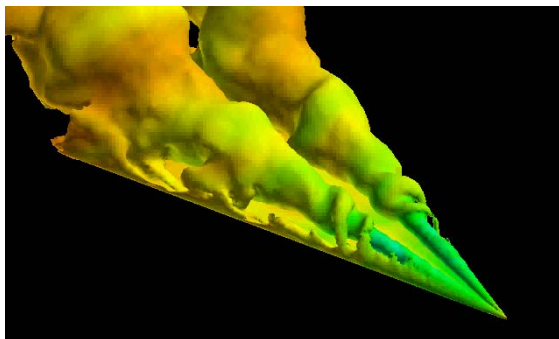
**Figure 10. Interaction between shear layer, secondary vortex, and primary vortex.**

Unforced Flowfield Results

Figure 11 shows the experimental average vorticity without periodic suction and blowing in a crossflow plane located at $x/c = 0.4$ (just prior to vortex burst). The primary and secondary vortices are visible, with the highest vorticity visible near the center of the primary vortex. ($2z/b = 0.37$ and $2y/b = 0.62$).
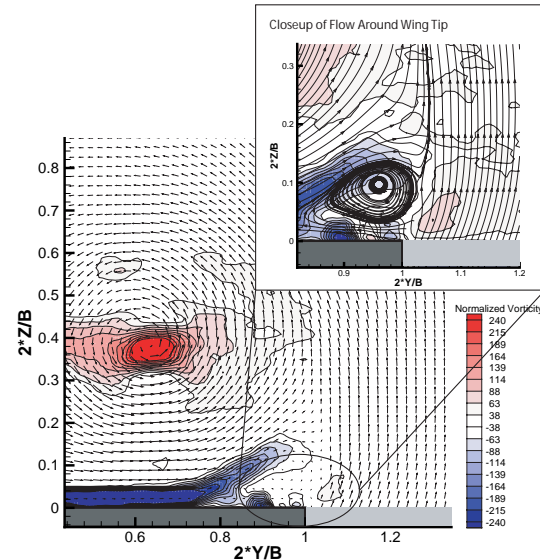
Figure 11. Experimental average vorticity without forcing at $x/c = 0.4$.

Figure 12 shows the computational equivalent of the experimental results presented near the wing-tip in Fig. 11. High vorticity is seen in the shear layer at the sharp leading-edge, with the primary vortex clearly wrapping up from the shear layer. The secondary vortex is also visible under the primary vortex (colored in blue due to its clockwise rotation).
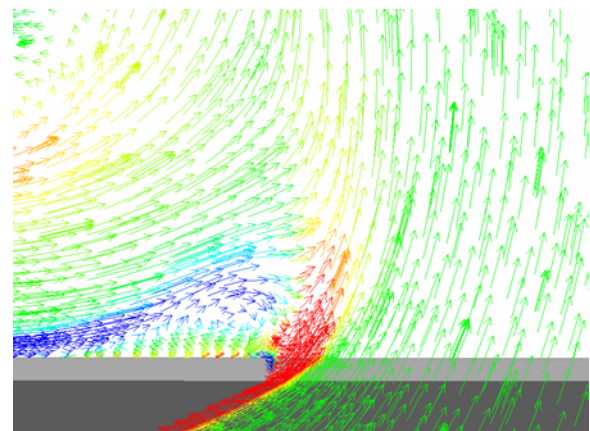
**Figure 12. Computational velocity vectors colored by x-vorticity without forcing at $x/c = 0.4$.**

Figure 13 shows a number of crossflow planes colored by x-vorticity and the delta wing surface colored by pressure. The first two crossflow planes ($x/c = 0.17$ and $x/c = 0.42$) show coherent vortices, but the final two planes ($x/c = 0.67$ and $x/c = 1.0$) clearly show that vortex breakdown has taken place.
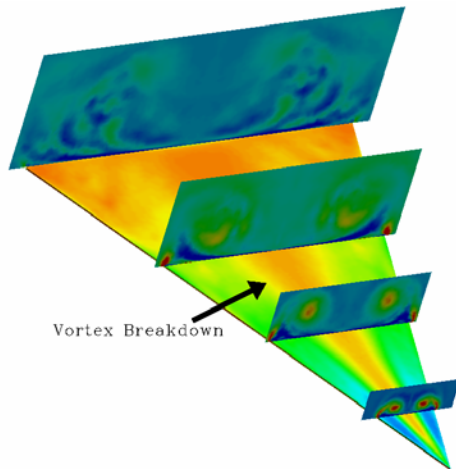
Figure 13. Computational crossflow planes of x-vorticity located at $x/c = 0.17, 0.42, 0.67,$ and 1.0. Delta wing surface colored by pressure.

A comparison of the unforced vortex core velocities with those from the computations is shown in Fig. 14. The experiment shows the vortex burst taking place from $x/c = 0.35$ to $x/c = 0.4$, while the instantaneous computation shows the burst taking place approximately 10% of the wing chord further aft. It should be noted that the computation for this case is highly unsteady, and the burst location is moving fore and aft on the wing. The computational results shown here are for one instant in time.
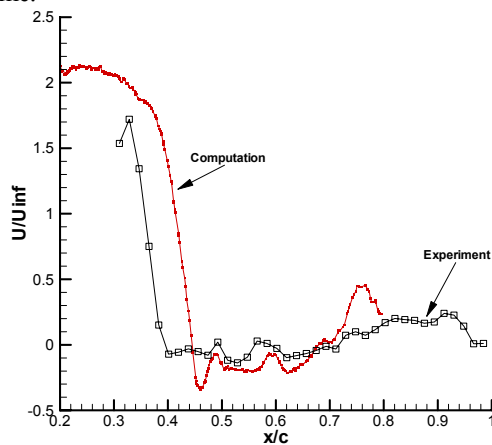

Figure 14. Computational and experimental axial velocity development along the vortex core (unforced).

Periodic Suction and Blowing

The experiment attempted to model the periodic suction and blowing as shown in Fig. 15 and given by

$$V = V_o \sin(\omega t)$$

The flowfield that results from this disturbance is hopefully altered in such as way as to increase the lift on the delta wing at high angles of attack.
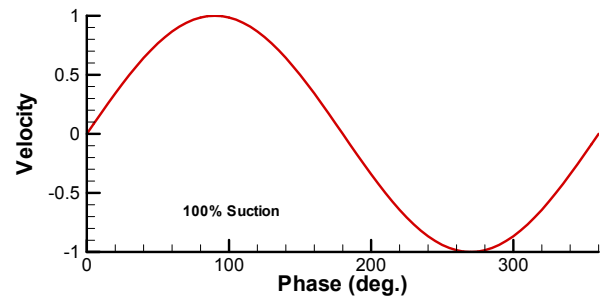

Figure 15. Ideal sinusoidal suction and blowing.

Once the periodic suction and blowing is begun the primary vortex begins to move around as vortices created by the suction and blowing interact with the primary vortex. The experimental location of the primary vortex center throughout a forcing cycle is shown in Fig. 16. Also included is the computational result for the no PSB location of the vortex core. The vortex core location was determined using an algorithm contained with the Fieldview post-processing software. The location matches the experimental value to within 4% of the local wing span, which we consider to be a very good simulation. The unforced vortex core location was taken from a single time step in the solution, and since the $x/c = 0.4$ axial plane is very near to the point of vortex burst, this location of the vortex core in the computations is unsteady.
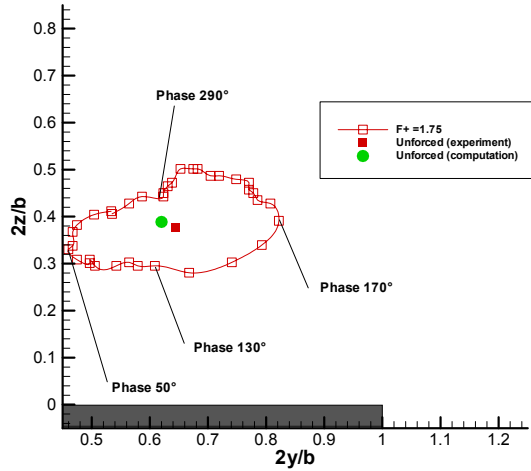
Figure 16. Experimental location of main vortex center during the forcing cycle. *x/c = 0.4, phase averaged data over 10 forcing cycles.*

Figure 17 shows the change in the vortex at x/c = 0.4 as a function of the blowing cycle. Recall that a phase of 90° represents full blowing, while a phase of 270° represents full suction. During the blowing phase, the leading-edge shear layer is canted to the right and the vortex core is drawn to the right. Evidence of a shear layer vortex forming is evident as well. By the time the suction phase has reached its peak, the vortex core has moved back to the left, as the shear layer is no longer being affected by the suction to any great extent.
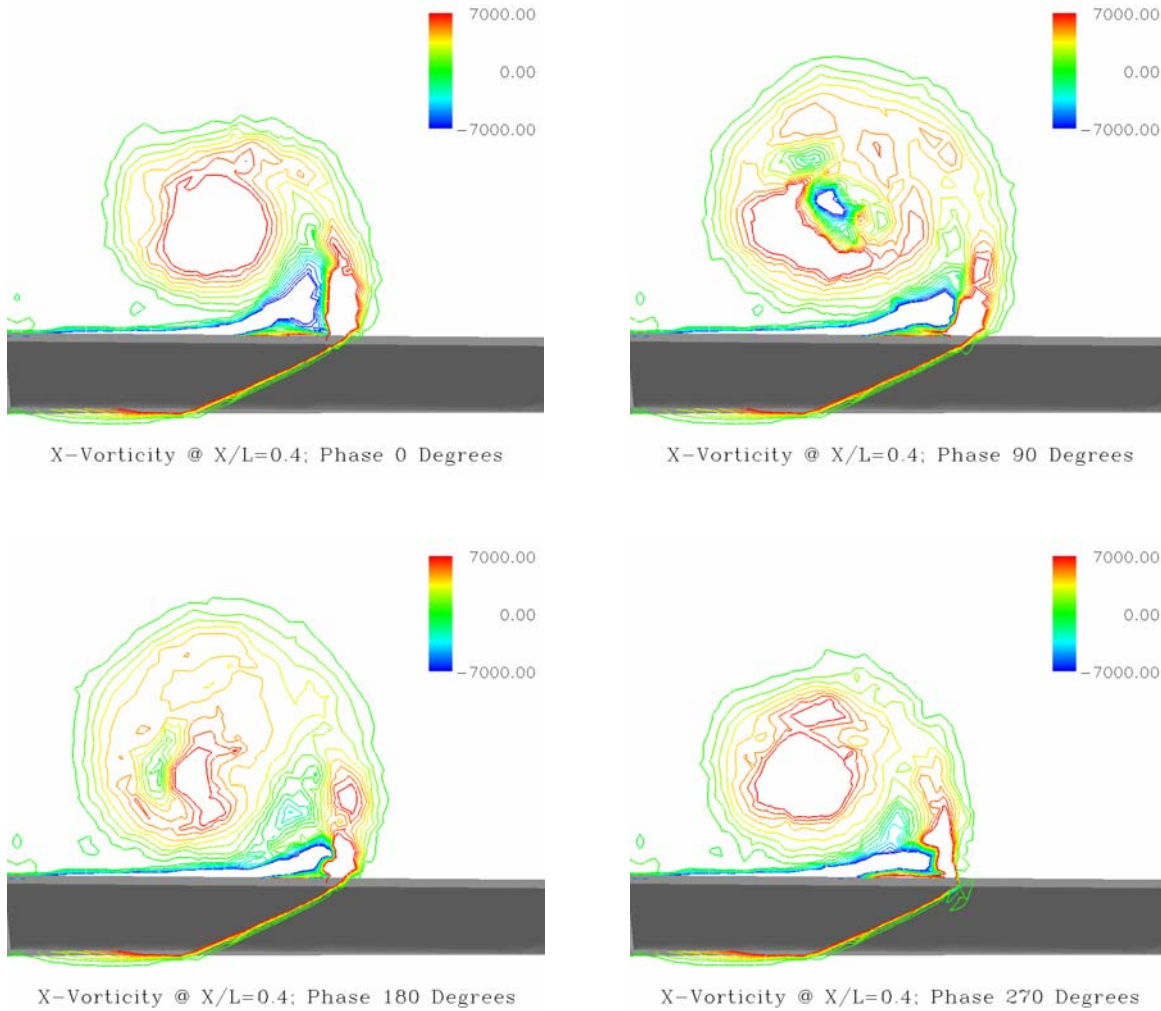
Figure 17. Computational prediction of vortex during the forcing cycle. *x/c = 0.4.*

The experimental velocity along the vortex core shown in Fig. 18 indicates that for the unforced case a stagnant or slightly reversed flow develops around $x/c = 0.4$. This coincides with the location at which the vorticity in the unforced flow drops, between $x/c = 0.4$ and $x/c = 0.5$. For the forced flow, however, the location of a drop in axial velocity is dependent on the phase within the forcing cycle. For two of the phase angles investigated, 130° and 170°, no stagnant flow can be observed over the entire wing. At these phase angles, the shear layer vortex generated by the forcing is present in the flow. In the absence of the shear layer vortex, at phase angles of 50° and 290°, the forced flow does show a significant drop in axial velocity, at locations of $x/c = 0.45$ and 0.55, respectively. One possible explanation for this behavior is that the shear layer vortex entrains fluid with high axial momentum from outside the wake left from the main vortex breakdown and thus increases the axial velocity. This would explain the decreased surface pressure found by Guy, et al., extending well downstream of their observed vortex breakdown location of $x/c = 0.75$.
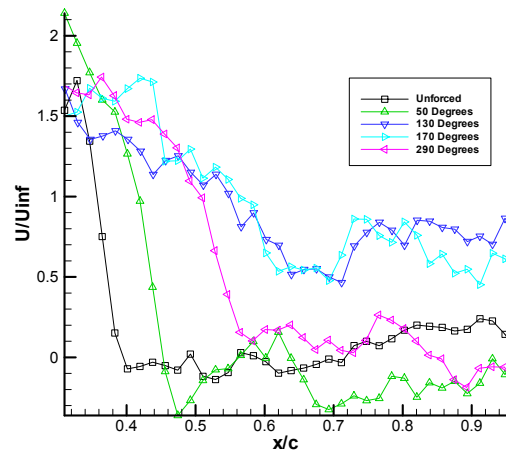
**Figure 18. Experimental axial velocity development along the vortex core.**

The experimental velocity profiles normal to the wing surface shown in Fig. 19 indicate that at $x/c = 0.60$ the axial velocity near the wing surface is higher even for phase angles (50° and 290°) in which a large decrease in axial velocity can be found upstream of this location. While the decrease in axial velocity is almost as large or even larger than for the unforced case, it is shifted about 0.05 chords away from the wing surface. Therefore higher velocity fluid is close to the wing, increasing the local velocity and presumably decreasing the surface pressure. This explains the total increase in normal force found in previous studies.
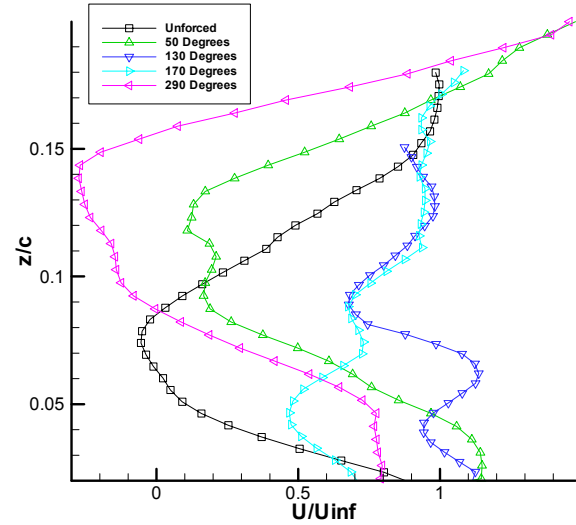
Figure 19. Experimental axial velocity profiles at x/c = 0.6.

One of the purposes of conducting a numerical simulation of the periodic suction and blowing is to determine information that would be unavailable in most experimental settings. The PIV experiment determined a great deal of information, but the computational results add to that information, and perhaps better inform future experiments. Figure 20 shows crossflow planes at $x/c = 0.6$, which adds to the understanding of the experimental results in Fig. 19. The blowing phase of the PSB cycle is able to reestablish the primary and secondary vortex structure to some extent, enabling the higher velocity fluid to remain closer to the surface of the wing.
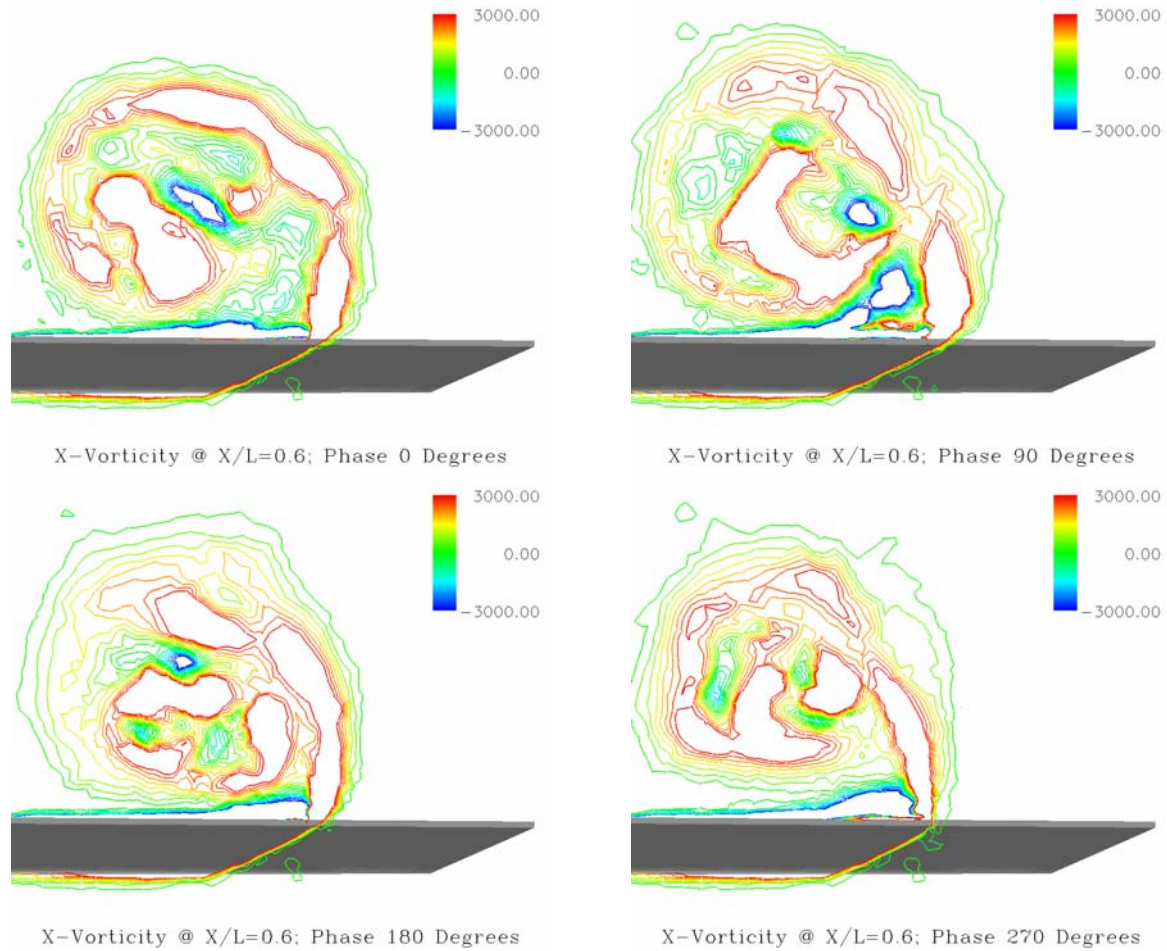
Figure 20. Computational prediction of vortex during the forcing cycle. *x/c* = 0.6.

Figure 21 shows the normal force acting on the delta wing. Initially the periodic suction and blowing is turned off (unforced case), and at approximately 29,800 iterations the periodic suction and blowing is initiated. There are a variety of interesting details that can be seen when comparing the two cases. As the periodic suction and blowing is initiated the average normal force acting on the delta wing increased from 0.945 N to 0.987 N— just under a 5% increase in normal force. In addition, the unforced case has a fairly low primary non-dimensional frequency of $F^+ = 0.221$, which is caused by the winding of the burst vortex. The primary frequency increases to $F^+ = 1.75$ when the periodic suction and blowing is initiated, which is the frequency of the suction and blowing.   While the forced case seems to provide improved lifting characteristics (on the average), in fact the fluctuations in normal force also increase as the suction and blowing is initiated. Peaks in normal force as high as 1.15 N can be seen in Fig. 21, but valleys as
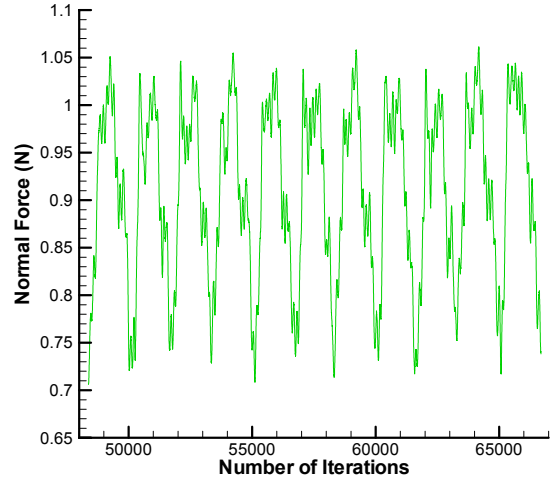
low as 0.8 N are also visible. Whether this represents an improvement in wing lifting characteristics is open to debate. The highly oscillatory nature of the forced case might make periodic suction and blowing impractical for everyday use unless some method controlling the force variations is determined.
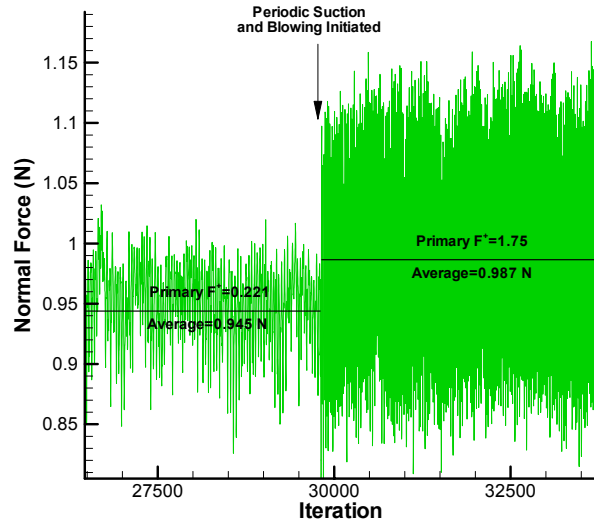
Figure 21. Normal force variation as periodic suction and blowing is initiated.

Figure 22. Normal force variation for periodic suction and blowing, $\Delta t^*=0.006$.

The double frequencies for the converged PSB case are easily seen in Fig. 22, which shows the normal force variation for 17,000 iterations (over ten cycles of the suction and blowing). Both the suction and blowing frequency is obvious, but overlayed on that frequency is the shear-layer instability frequency, constantly oscillating around the lower frequency. The average normal force is now 0.921 N, which is even lower than the unforced case. This difference may be due to the different time steps used and should not be used to draw conclusions. Notice that the blowing portion of the suction/blowing cycle is more effective, as evidenced by the amount of time the normal force remains at the highest levels. When the suction cycle takes place, decreasing the normal force, the force spikes to a minimum value but then quickly rises again as the suction phase ends. This explains why, during the experimental portion of this work, it appeared that the suction was incomplete (or possibly working incorrectly). Even the numerical simulation clearly shows that the suction phase is not as effective in altering the normal force acting on the delta wing.

Closeups of the flowfield in the vicinity of the slot help to explain the results of Fig. 22. Figure 23 shows velocity vectors colored by *x*-vorticity for two phases of the PSB cycle. It is clearly evident that the blowing phase is affecting a large change to the velocity field in the vicinity of the slot, while the suction phase is not nearly as affective. This is probably due to the difficulty the suction has in forcing the crossflow to turn the corner into the slot, while the blowing is enhancing the upward direction of the crossflow. In fact, the suction seems to turn more air upward than into the slot. Future slot configurations should take this into account.
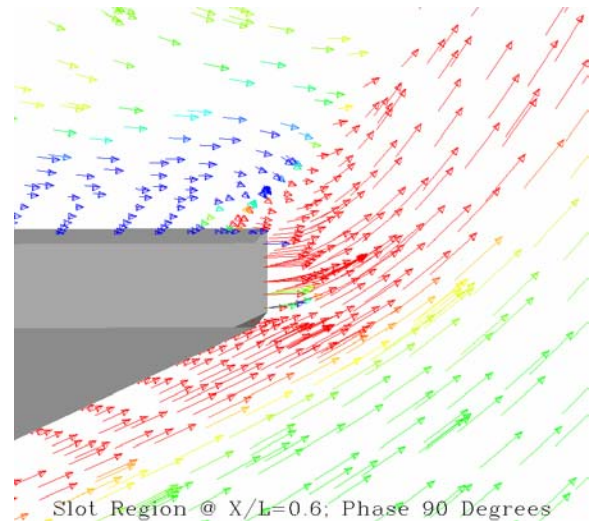
a) blowing phase
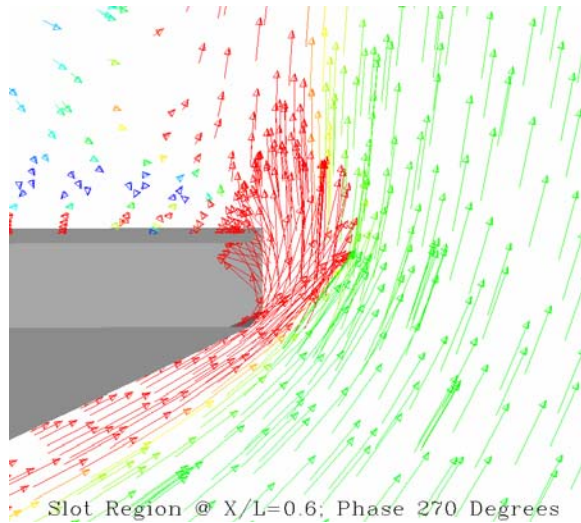
b) suction phase

Figure 23. Velocity vectors in the vicinity of the slot colored by *x*-vorticity, *x/c* = 0.6.

Conclusions

The flow over a 70° delta wing at a chord Reynolds number of 40,700 and an angle of attack of 35° was investigated in a water tunnel experiment and by a numerical simulation. The flow was forced using periodic suction and blowing along the entire leading edge at a non-dimensional frequency of $F+ = 1.75$. It was found that periodic suction and blowing does not delay vortex breakdown a great deal, with vortex breakdown taking place between $x/c = 0.4$ and 0.5 for both the forced and unforced case, as evidenced by a drop in vorticity by almost an order of magnitude. For the unforced flow the location of the drop in streamwise vorticity was found to coincide with a drop in axial velocity. For the forced flow the location where the axial velocity dropped abruptly was fluctuating throughout the forcing cycle between $x/c = 0.45$ and downstream of the trailing edge. The forcing resulted in an overall increase in axial velocity in the vortex core near the wing surface, especially beyond vortex breakdown.

Since forcing does not appear to improve the flow upstream of vortex breakdown, future experiments are planned to investigate the effect of forcing along portions of the leading edge instead of the entire leading edge. Also, forcing methods that may improve the location of vortex breakdown by altering the shape of the vortex core from straight to curved by using spatially modulated forcing upstream of the natural vortex breakdown location are being considered.

A critical examination of the results obtained from a numerical simulation of the flow field on a delta wing with periodic suction and blowing was also presented. The results indicate that the computational scheme properly captured the effect of periodic suction and blowing on the main parameters of the flowfield and on the normal force of the delta wing. The numerical results enabled the researchers to investigate a variety of flowfield details that were not known from the experiments, including the frequency of the vortex breakdown winding, the incremental change in normal force on the delta wing due to periodic suction and blowing, the oscillatory behavior of the force acting on the delta wing, and the impact of the periodic suction and blowing on the burst vortex winding frequency. In addition, the numerical simulation was suggested as a method to verify difficulties in the experiment, such as the possibility of the suction cycle not being fully realized.

A great deal of value can be achieved when experiments and computations are used in a synergistic fashion. Each approach has its strengths and weaknesses, and by employing the strengths of both experiments and computations in solving an aerodynamic problem, a more complete and full picture of the processes of aerodynamics will be more realized.

References

1.   Ekaterinaris, J.A., Coutley, R.L., Schiff, L.B., and Platzer, M.F., "Numerical Investigation of High Incidence Flow Over a Double-Delta Wing," *Journal of Aircraft*, Vol. 32, No. 3, 1995, pp. 457-463.

2.   Murman, S., Rizk, Y.M., Cummings, R.M., and Schiff, L.B., "Computational Investigation of Slot Blowing for Fuselage Forebody Flow Control," *Aircraft Design,* Vol. 2, No. 1, 1999, pp. 45-63.

3.   Huang, X.Z., Lui, T.C., and Hanff, E.S., "A Novel Concept for Controlling Leading-Edge Vortex Breakdown and Related Preliminary Water Tunnel Experiment," AIAA Paper 2001-4143, Aug. 2001.

4.   Mitchell, A.M. and Delery, J., "Research Into Vortex Breakdown Control," *Progress in Aerospace Sciences*, Vol. 37, No. 4, 2001, p. 385-418.

5.   Mitchell, A.M., Barber, D., Molton, P., and Delery, J., "Oscillation of Vortex

Breakdown Location and Blowing Control of Time-Averaged Location," *AIAA Journal*, Vol. 38, No. 5, 2000, pp. 793-803.

6. Visbal, M. R: "Computational and Physical Aspects of Vortex Breakdown on Delta Wings," AIAA Paper 95-0585, Jan. 1995.

7. Agrawal, S.A., and Barnett, R., "Numerical Investigation of Vortex Breakdown on a Delta Wing," *AIAA Journal*, Vol. 30, No. 3, 1992, pp. 584-591.

8. Iwanski, K.P., Ng, T.T., and Nelson, R.C., "An Experimental Investigation of Delta Wing Vortex Flow With and Without External Jet Blowing," AIAA Paper 89-0084, Jan. 1989.

9. Guy, Y., Morrow, J.A., and McLaughlin, T.A., "Control of Vortex Breakdown on a Delta Wing by Periodic Blowing and Suction," AIAA Paper 99-0132, Jan. 1999.

10. Guy, Y., Morrow, J.A., McLaughlin, T.A., and Wygnanski, I., "Pressure Measurement and Flow Field Visualization on a Delta Wing with Periodic Blowing and Suction," AIAA Paper 99-4178, Aug. 1999.

11. Guy, Y., Morrow, J.A., McLaughlin, T.A., and Wygnanski, I., "Parametric Investigation of the Effects of Active Control on the Normal Force on a Delta Wing," AIAA Paper 2000-0549, Jan. 2000.

12. Guy, Y., Morrow, J.A., McLaughlin, T.A., and Wygnanski, I., "Velocity Measurements on a Delta Wing with Periodic Blowing and Suction," AIAA Paper 2000-0550, Jan. 2000.

13. Morton, S. A., Guy, Y., Morrow, J.A., and Blake, D.C., "Numerical Simulation of Periodic Suction and Blowing Control of Vortex Breakdown on a Delta Wing," AIAA Paper 99-3195, June 1999.

14. Siegel, S.G., McLaughlin, T.E., and Morrow, J.A., "PIV Measurements on a Delta Wing with Periodic Blowing and Suction," AIAA Paper 2001-2436, June 2001.

15. Strang, W. Z., Tomaro, R. F, and Grismer, M. J., "The Defining Methods of Cobalt$_{60}$:

A Parallel, Implicit, Unstructured Euler/Navier-Stokes Flow Solver," AIAA Paper 99-0786 Jan. 1999.

16. Tomaro, R.F., Strang, W. Z., and Sankar, L. N., "An Implicit Algorithm for Solving Time Dependent Flows on Unstructured Grids," AIAA Paper 97-0333, Jan. 1997.

17. Grismer, M. J., Strang, W. Z., Tomaro, R. F., and Witzemman, F. C., "Cobalt: A Parallel, Implicit, Unstructured Euler/Navier-Stokes Solver," *Advances in Engineering Software*, Vol. 29, No. 3-6, 1998, pp. 365-373.

18. Forsythe, J.R., Strang, W., Hoffmann, K.A., "Validation of Several Reynolds-Averaged Turbulence Models in a 3D Unstructured Grid Code," AIAA Paper 2000-2552, June 2000.

19. Morton, S.A., Guy, Y., Morrow, J.A., and Blake, D.C., "Numerical Simulation of Periodic Suction and Blowing Control of Vortex Breakdown on a Delta Wing," AIAA Paper 99-3195, June 1999.

20. Guy, Y., Morton, S.A., and Morrow, J.A., "Numerical Investigation of the Flow Field on a Delta Wing with Periodic Blowing and Suction," AIAA Paper 2000-2321, June 2000.

21. Cummings, R.M., Morton, S.A., Siegel, S.G., McLaughlin, T.E., and Albertson, J.A., "Combined Computational Simulation and PIV Measurements on a Delta Wing with Periodic Suction and Blowing," AIAA Paper 2002-0300, Jan. 2002.

22. Barberis, D., Quelin, C., and Petit, S., "Contrôl de L'éclatement Tourbillonnaire Sur L'aile AFV-D60^o au Tunnel Hydrodynamique TH2," ONERA Technical Report RT 136/03582 DAFE, March 2001.

23. Gad-el-Hak, M., and Blackwelder, R.F., "The Discrete Vortices From a Delta Wing," *AIAA Journal*, Vol. 23, No. 6, 1985, pp. 961-962.

24. Lowson, M.V., "The Three Dimensional Vortex Sheet Structure on Delta Wings," AGARD Conference Proceedings No. 438, Oct. 1988, pp. 11.1-11.16.